Title	Orthorhombic distortion-induced anatase-like optoelectronic properties of rutile TiO2
Author(s)	Chen, Binjie; Kang, Kungwan; Jeen, Hyoungjeen et al.
Citation	Journal of Applied Physics, 132(18), 185301 https://doi.org/10.1063/5.0119725
Issue Date	2022-11-14
Doc URL	https://hdl.handle.net/2115/90698
Rights	This article may be downloaded for personal use only. Any other use requires prior permission of the author and AIP Publishing. This article appeared in Binjie Chen, Kungwan Kang, Hyoungjeen Jeen, Yuqiao Zhang, Jinghuang Lin, Bin Feng, Yuichi Ikuhara, Sena Hoshino, Katsuyuki Matsunaga, and Hiromichi Ohta , "Orthorhombic distortion-induced anatase-like optoelectronic properties of rutile TiO2", Journal of Applied Physics 132, 185301 (2022) https://doi.org/10.1063/5.0119725 and may be found at https://doi.org/10.1063/5.0119725
Type	journal article
File Information	5.0119725.pdf

Journal of Applied Physics

Orthorhombic distortion-induced anatase-like optoelectronic properties of rutile TiO_2

Cite as: J. Appl. Phys. **132**, 185301 (2022); https://doi.org/10.1063/5.0119725
Submitted: 10 August 2022 • Accepted: 16 October 2022 • Published Online: 08 November 2022

Binjie Chen, Kungwan Kang, Hyoungjeen Jeen, et al.

AIP Publishing

Journal of Applied Physics
ARTICLE
scitation.org/journal/jap

Orthorhombic distortion-induced anatase-like optoelectronic properties of rutile TiO_2

Cite as: J. Appl. Phys. **132**, 185301 (2022); doi: 10.1063/5.0119725
Submitted: 10 August 2022 · Accepted: 16 October 2022 ·
Published Online: 8 November 2022

Binjie Chen,[1,a)] Kungwan Kang,[2] Hyoungjeen Jeen,[2] Yuqiao Zhang,[3,4] Jinghuang Lin,[5] Bin Feng,[5] Yuichi Ikuhara,[5] Sena Hoshino,[6] Katsuyuki Matsunaga,[6] and Hiromichi Ohta[7,a)]

AFFILIATIONS

[1] Graduate School of Information Science and Technology, Hokkaido University, N14W9, Kita, Sapporo 060-0814, Japan
[2] Department of Physics, Pusan National University, Busan 46241, South Korea
[3] Institute of Quantum and Sustainable Technology (IQST), School of Chemistry and Chemical Engineering, Jiangsu University, Zhenjiang 212013, China
[4] Foshan (Southern China) Institute for New Materials, Foshan 528200, China
[5] Institute of Engineering Innovation, The University of Tokyo, 2-11-16 Yayoi, Bunkyo, Tokyo 113-8656, Japan
[6] Department of Materials Physics, Nagoya University, Furo, Chikusa, Nagoya 464-8603, Japan
[7] Research Institute for Electronic Science, Hokkaido University, N20W10, Kita, Sapporo 001-0020, Japan

[a)] **Authors to whom correspondence should be addressed:** binjie.chen.t7@elms.hokudai.ac.jp and hiromichi.ohta@es.hokudai.ac.jp

ABSTRACT

Titanium dioxide (TiO_2) is an excellent photocatalyst and transparent conducting oxide. It has two major crystal structures: rutile and anatase. Anatase TiO_2 is valuable from an industrial point of view because it typically displays better photocatalytic and electronic transport properties than rutile TiO_2. To further extract the functional properties of TiO_2, understanding the correlation between the electronic structure and the crystal structure is essential. Because the electronic structure strongly depends on the crystal structure, introducing lattice distortion to rutile TiO_2 should effectively modulate its electronic structure. Here, we show that Nb-doped rutile TiO_2 epitaxial films on $(1\bar{1}00)$ α-Al_2O_3 substrates exhibit anatase-like optoelectronic properties due to orthorhombic lattice distortions and experimentally observe the change in the electronic structure. Reducing the film thickness increases the orthorhombic distortion ratio (b/a) up to 3.4%. As b/a increases, the carrier effective mass decreases from 35 to 3 m_0 (m_0: electron mass) and the optical bandgap significantly increases. The present observations provide insight into regulating the TiO_2 physical properties and should be beneficial for designing TiO_2-based photocatalysts and transparent conducting electrodes.

I. INTRODUCTION

Titanium dioxide (TiO_2) is an active material for photocatalytic water splitting. The optical bandgap (E_g) of TiO_2 is 3.1–3.3 eV, which is close to the maximum energy of visible light (~3.1 eV).[1–3] Fundamentally, the E_g of TiO_2 is composed of a Ti 3d-based conduction band minimum (CBM) and an O 2p-based valence band maximum (VBM). When TiO_2 absorbs light (photon energy $> E_g$), the valence electron is excited to the conduction band, generating a positive hole in the valence band. The conduction electron reduces water while the hole oxidizes it.[4–7] In addition, the photocatalytic activity strongly depends on the crystal structure of TiO_2 because the electronic structure is affected by the crystal structure.[8–12] Thus, understanding the correlation between the electronic and crystal structures is essential to extract the functional properties of TiO_2.

TiO_2 has a series of stable polymorphs in nature, e.g., rutile, anatase, brookite, etc. Among them, rutile and anatase are the most thermodynamically stable and representative. Rutile is the most stable phase at high temperatures. Anatase is stable at low temperatures but changes into the rutile phase when heated up above 600 °C.[13,14] The photocatalytic activity of the anatase phase is an order of magnitude higher than that of the rutile phase,[11,15] possibly due to higher mobility and the nature of indirect bandgap. Still due to the conduction electrons of the anatase phase having a higher mobility than those of the rutile phase,[16,17] it is more suitable as transparent conducting oxide (TCO) when donor dopants are doped. Therefore, anatase TiO_2 is more valuable than rutile TiO_2 from an industrial point of view.

To clarify the difference, high-quality epitaxial films of TiO_2 are useful. Although high-quality anatase TiO_2 can be heteroepitaxially grown on several perovskite oxide substrates ($SrTiO_3$ and $LaAlO_3$) at high temperatures ($T_g \sim 700\,°C$),[18–21] fabricating large-area films is difficult due to the size limitation of the substrates. This study focuses on the anisotropic crystal structure of α-Al_2O_3 substrates. Figure 1 depicts the lattices of (001) rutile TiO_2 and $(1\bar{1}00)$ α-Al_2O_3 crystals. The epitaxial relationship is (001) [100] TiO_2 || $(1\bar{1}00)$ [0001] α-Al_2O_3.[22–24] Due to the anisotropic lattice parameter of $(1\bar{1}00)$ α-Al_2O_3 in the in-plane directions, the rutile TiO_2 lattice sustains compressive strain along [100] (lattice mismatch: + 5.9%), whereas tensile strain occurs along [010] (lattice mismatch: −3.5%). Because the electronic structure strongly depends on the crystal structure, introducing lattice distortion to rutile TiO_2 should effectively modulate its electronic structure.

Here, we show that electron-doped rutile TiO_2 epitaxial films on $(1\bar{1}00)$ α-Al_2O_3 substrates exhibit anatase-like optoelectronic properties, presumably due to orthorhombic lattice distortions. In addition, we demonstrate that the TiO_2 film thickness controls the degree of orthorhombic distortion. The present observations provide insight into regulating the physical properties of TiO_2 and should be beneficial for designing TiO_2-based photocatalysts and transparent conducting electrodes.

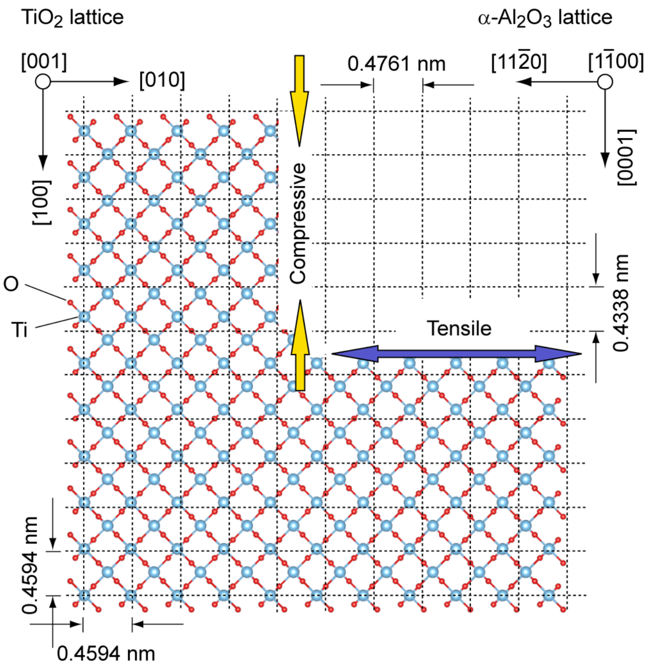

FIG. 1. Hypothesis of the orthorhombic lattice distortion of the rutile-structured TiO_2 epitaxial film on an M-plane sapphire substrate. Schematic of the crystal lattice of rutile TiO_2 on $(1\bar{1}00)$ α-Al_2O_3 (sublattice of oxide ions, dotted lines). Since lattice parameter a of TiO_2 is longer than lattice parameter c of α-Al_2O_3 (lattice mismatch: −5.9%), compressive strain is assumed, whereas the tensile strain is assumed because lattice parameter a of α-Al_2O_3 is larger than that of the lattice parameter b of TiO_2 (lattice mismatch: +3.5%). Therefore, we hypothesized that orthorhombic distortion is introduced in the TiO_2 lattice. For convenience, the TiO_2 lattice is represented by the ball and stick model, while the α-Al_2O_3 lattice is simplified to the sublattice of oxide ions, which is shown by the dotted lines.

II. EXPERIMENTAL SECTION

A. Sample preparation

The target was a 0.5%-Nb-doped TiO_2 ceramic disk. Pulsed laser deposition (PLD) with a KrF excimer laser ($\lambda = 248$ nm, laser fluence ~ 1 J cm^{-2} pulse^{-1}, and repetition rate = 10 Hz) was used to fabricate 0.5%-Nb-doped TiO_2 films on $(1\bar{1}00)$ α-Al_2O_3 single crystal substrates, where the slight doping is to provide the donor dopant to facilitate further electronic measurements. Such low-level doping does not affect the lattice structure significantly.[25,26] During film growth, the substrate temperature and oxygen pressure were kept constant at 500 °C and 5×10^{-3} Pa, respectively. Adjusting the deposition time controlled the film thickness.

B. Crystallographic analyses

The film thickness, crystallographic orientations, and lattice parameters were determined using high-resolution x-ray diffraction (XRD, ATX-G, Rigaku) with Cu Kα_1 ($\lambda = 0.154\,059$ nm) radiation. Both out-of-plane and in-plane measurements were performed to extract the lattice parameters. The atomic arrangement of the resultant films was visualized using STEM (ARM200CF, JEOL Co. Ltd) operated at 200 keV. HAADF-STEM images were taken with a detection angle of 68–280 m rad.

All measurements were conducted at room temperature.

C. Electrical and optical properties' measurements

The electrical resistivity (ρ), carrier concentration (n), and Hall mobility (μ_{Hall}) at room temperature were measured by the dc four-probe method with the van der Pauw electrode configuration in air. The temperature-dependent electrical resistivity ($\rho - T$), carrier concentration ($n - T$), and Hall mobility ($\mu_{Hall} - T$) were performed using the same configuration in a vacuum and a variable temperature of 10–300 K. The thermopower (S) of the films in the in-plane direction was measured by the conventional steady-state method. The transmission and reflection spectra in the 200–1600 nm wavelength range were measured by a spectrophotometer (SolidSpec-3700, Shimadzu).

D. X-ray absorption spectroscopy (XAS) measurements

XAS measurements were performed at the 2A beamline of the Pohang Accelerator Laboratory (PAL) with the grazing incidence (22.5°) configuration in the total-electron-yield (TEY) mode. The Ti L-edge spectra were measured at room temperature.

E. Density functional theory (DFT) calculations

DFT calculations were performed with the projector-augmented wave method implemented in the Vienna *Ab initio* Simulation Package (VASP) program.[27,28] For the exchange-correlation term of the electrons, the generalized gradient approximation (GGA) parameterized by Perdew, Burke, and Ernzerhof was used.[29] The electrons

TABLE I. Calculated effective masses for electrons in non-distorted (case 1) or orthogonally distorted (cases 2 and 3) rutile TiO_2.

	Effective mass m^*/m_0			
	Γ→X	Γ→Y	Γ→M	Γ→S
Case 1 (a_0, $b_0 = a_0$, c_0)	1.672		0.588	
Case 2 (a_0, $b_0 = 1.030a_0$, c_0)	1.777	1.698		0.656
Case 3 ($0.995a_0$, $b_0 = 1.030a_0$, $0.994c_0$)	1.759	1.664		0.742

were $3p^6$, $3d^2$, and $4s^2$ for Ti and $2s^2$ and $2p^4$ for O. To describe the localized features of the Ti 3d orbitals, the GGA + U method was employed, where the onsite Coulomb repulsion was considered with an effective parameter of $U = 7.0$ eV for Ti 3d.[30,31] Han *et al.* suggested the optimum choice of the U parameter for TiO_2.[31] The electronic wavefunctions were expanded by plane waves up to a cutoff energy of 500 eV. Brillouin zone integration was performed with the Monkhorst-Pack mesh of $4 \times 4 \times 6$ for the unit cell of rutile TiO_2. The structure was optimized until the atomic forces converged to less than 0.01 eV/Å. The calculated lattice parameters of $a = 0.469$ nm and $c = 0.305$ nm slightly overestimated the experimental data,[32] but the trends were similar to those in previous GGA calculations.[31]

The present GGA + U calculations indicated that rutile TiO_2 had a direct theoretical E_g of 2.30 eV at the Γ point (Fig. S1 in the supplementary material). To evaluate effective masses (m^*) of electrons in rutile TiO_2, the energy dispersion curves at the CBM were obtained around the Γ point for the rutile TiO_2 unit cell (structure-optimized as above) using a k-point mesh density toward a particular symmetric point of more than 4.2 nm. Subsequently, parabolic curve fitting for five k-points centered at Γ was performed, and the m^* values of electrons were obtained from the second partial derivatives of the parabolic fitting curves.[33]

Although the theoretical E_g (2.30 eV) of bulk rutile TiO_2 underestimated the experimental value (3.03 eV),[34] which is a standard feature of GGA-related DFT calculations, such a small theoretical E_g may also affect the theoretical m^*. To evaluate the effect of the theoretical E_g on m^*, hybrid-functional calculations only at the Γ point were also performed using the hybrid density functional proposed by Heyed, Scuseria, and Ernzerhof (HSE06).[35,36] The E_g of 3.20 eV calculated by HSE06 reproduced the experimental E_g value better than that by the GGA + U calculations. However, the calculated m^* of 1.168 for Γ to X and 0.414 for Γ to M were slightly smaller than the corresponding GGA + U values of 1.672 and 0.588, respectively (Table I). However, these differences do not affect the conclusion of this paper. Since hybrid-functional calculations are computationally demanding, the GGA + U calculations were mainly used to investigate m^* in distorted rutile TiO_2.

III. RESULTS AND DISCUSSIONS

A. Epitaxial film growth of rutile Nb:TiO_2 with orthorhombic distortion

Figure 2 summarizes the crystallographic characterization of the resultant Nb:TiO_2 films on $(1\bar{1}00)$ α-Al_2O_3 substrates. The out-of-plane XRD patterns exhibit intense 002 diffraction peaks of rutile Nb:TiO_2 and those of $3\bar{3}00$ α-Al_2O_3 substrate [Fig. 2(a)], indicating a high c-axis orientation. As the thickness increases, the 002 peak shifts toward the smaller scattering vector and approaches the bulk position (dashed line), which suggests an increasing trend of the lattice parameter c [Fig. 2(c)]. The in-plane XRD patterns [Fig. 2(b)] have different peak positions for the 400 (upper) and the 040 (lower). The 400 diffraction peaks of Nb:TiO_2 are seen together with those of $00\,0\underline{12}$ α-Al_2O_3 substrates at $\sim q_x/2\pi = 8.75\ \mathrm{nm}^{-1}$. This is slightly larger than that of bulk (dashed line), but the 400 peaks are independent of thickness. In contrast, the 040 diffraction peaks of Nb:TiO_2, which are seen together with $22\bar{4}0$ α-Al_2O_3 substrates, shift toward a larger scattering vector as the thickness increases and approaches $\sim q_y/2\pi = 8.67\ \mathrm{nm}^{-1}$. This value is slightly smaller than that of the bulk (dashed line).

Figure 2(d) summarizes the in-plane lattice parameters a and b as functions of the film thickness. Note that the lattice parameters of the 10-nm-thick and 20-nm-thick samples were extracted from the 200 Nb:TiO_2 and 020 Nb:TiO_2 diffraction peaks due to the weak peak intensities of 400 Nb:TiO_2 and 040 Nb:TiO_2 (Fig. S2 in the supplementary material). Lattice parameter a is ∼0.457 nm, which is slightly shorter than that of the bulk (0.4594 nm) due to the compressive strain originating from the lattice mismatch (−5.9%). Lattice parameter a is independent of the thickness. Unlike lattice parameter a, lattice parameter b shows a clear thickness dependence. For a 10-nm-thick film, lattice parameter b is 0.473 nm, which is ∼3% longer than that of bulk rutile TiO_2. However, it decreases to 0.461 nm, which is slightly longer than that of the bulk when the thickness is 300 nm. This clearly indicates the presence of a strong tensile strain originating from the lattice mismatch (+3.5%) (Table II).

To visualize the orthorhombic lattice distortion, we defined the ratio of lattice parameters (b/a) as the degree of orthorhombic distortion [Fig. 2(e)]. The ratio b/a gradually decreases as the Nb:TiO_2 thickness increases and ranges from ∼1.035 to ∼1.01. It should be noted that the Nb:TiO_2 films were grown incoherently on $(1\bar{1}00)$ α-Al_2O_3 substrates (Figs. S3–S8 in the supplementary material). These results confirm that orthorhombic strain is successfully introduced to the rutile TiO_2 and that the strain becomes smaller as the thickness increases. Also note that the change tendency of lattice parameter b slowed down when the films are thicker than 100 nm, indicating such tensile strain has been highly weakened under this condition.

To further clarify the orthorhombic distortion, cross-sectional STEM images were acquired for 6- and 200-nm-thick TiO_2 films prepared under the same growth conditions. Figure 3 shows the high-resolution HAADF-STEM images along the [0001]Al_2O_3 zone axis and the corresponding inverse fast Fourier transformation (IFFT) images. HAADF-STEM images [Figs. 3(a) and 3(b)] exhibit a clear Z-contrast for the Ti and Al atoms. Consequently, the interface of TiO_2/M-plane sapphire can be observed, as shown by the dashed line.

Comparing the observed and theoretical structures of TiO_2 demonstrates that both the 6- and 200-nm-thick films show (001) oriented rutile structures, which is consistent with our XRD results. IFFT is an intuitive method for observing dislocations. The lack of dislocations in IFFT of the 6-nm-thick film indicates that the TiO_2

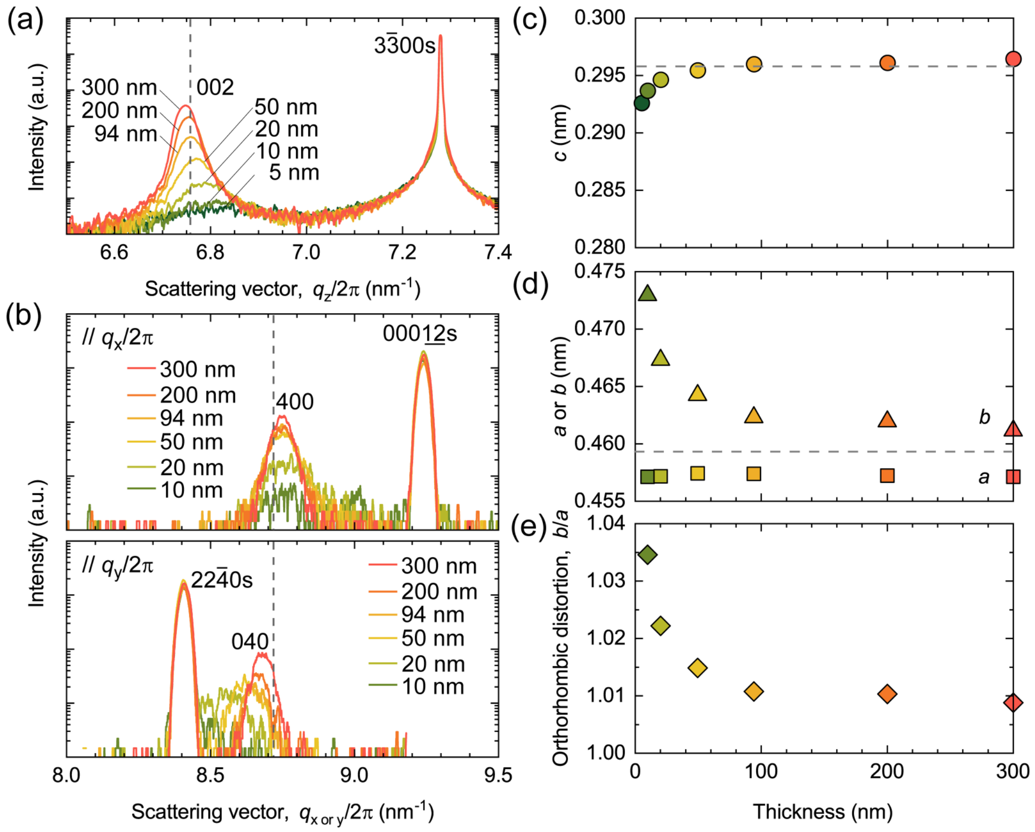

FIG. 2. Crystallographic characterization of the resultant TiO_2 films on an M-plane sapphire substrate. (a) Out-of-plane and (b) in-plane XRD patterns of 5–300-nm-thick TiO_2 films grown on a (1$\bar{1}$00) α-Al_2O_3 substrate. For the in-plane pattern, the upper and lower figures correspond to the XRD patterns among azimuth [0001] α-Al_2O_3 and azimuth [11$\bar{2}$0] α-Al_2O_3, respectively. Dotted lines indicate the position of bulk TiO_2. Thickness dependence of the (c) out-of-plane lattice parameter *c* and (d) in-plane lattice parameters *a* and *b*, which are extracted from the XRD patterns. Dotted lines indicate the lattice parameters of bulk TiO_2. (e) Orthorhombic distortion *b*/*a* of the resultant TiO_2 films.

lattice is strained [Fig. 3(c)]. In contrast, the edge dislocations at the interface of the 200-nm-thick film [Fig. 3(d)] suggest that the strain is released by forming dislocations. The uneven distribution of dislocations may be due to no post-annealing. Based on the dislocation observations, the orthorhombic distortion originates from the elastic deformation of the lattice and was relieved through dislocation formation. In addition, we also observed the HAADF-STEM images along the[11$\bar{2}$0]Al_2O_3 zone axis of these two films (Fig. S9 in the supplementary material). The existence of edge dislocations in both films along this direction is also well consistent with the smaller change tendency of lattice parameter *a* [Fig. 2(d)]. For the 200-nm-thick films, we also observed the lattice parameter difference along the out-of-plane. No clear atom spacing difference was observed, indicating that the strain release only occurs around the dislocation at the interface instead of a gradient release from the interface to the surface. Such phenomenon has been experimentally revealed by other reports,[37,38] and it also confirms the uniformity of the film.

TABLE II. The comparison of lattice mismatch and distortion along [0001] Al_2O_3 and [11$\bar{2}$0] Al_2O_3 direction.

Substrate orientation	0001	11$\bar{2}$0
Film orientation	100	010
Lattice mismatch	+5.9%	−3.5%
Lattice parameter of films	0.457 nm (10 nm) 0.457 nm (300 nm)	0.473 nm (10 nm) 0.461 nm (300 nm)
Relation between lattice parameter and thickness	Weak	Strong

B. Electrical and optical properties of the rutile Nb:TiO_2 films

The electron transport properties of the resultant Nb:TiO_2 films were measured at room temperature. Figure 4 summarizes the electron transport properties as a function of the

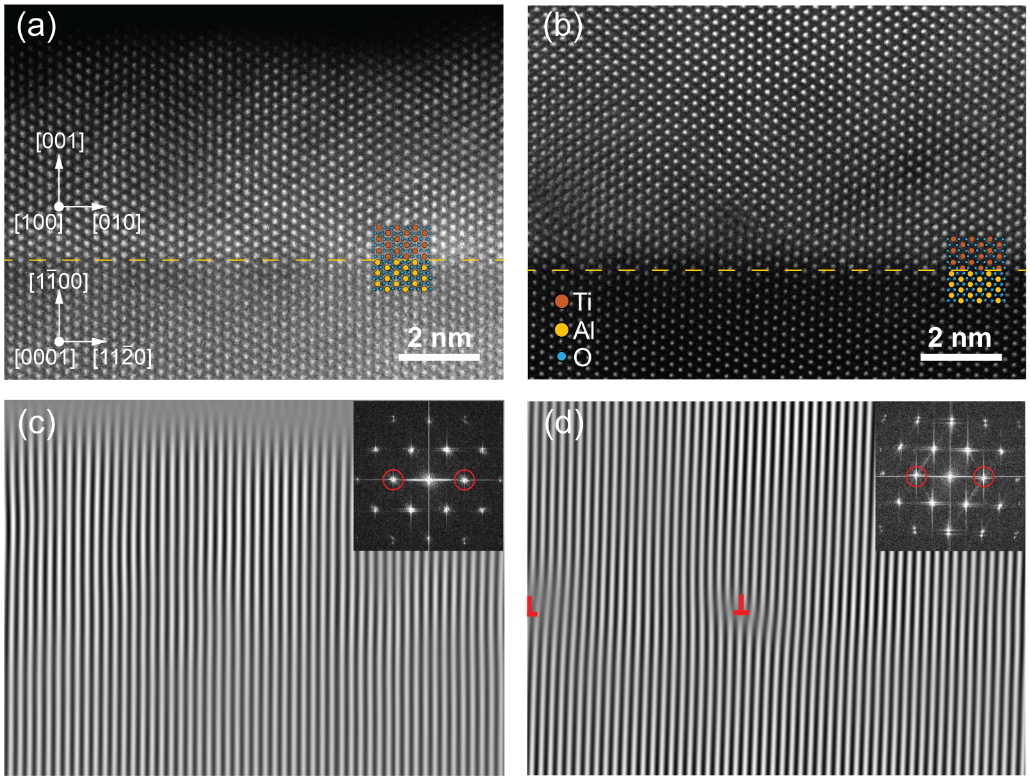

FIG. 3. Cross-sectional STEM images of the TiO_2 films on an M-plane sapphire substrate. (a) and (b) HAADF-STEM images of (a) 6-nm-thick and (b) 200-nm-thick TiO_2 films grown on (1$\bar{1}$00) α-Al_2O_3 substrates along the [0001]Al_2O_3 zone axis. The dashed line indicates the interface of TiO_2/α-Al_2O_3. (c) and (d) Corresponding IFFT images of (c) 6-nm-thick and (d) 200-nm-thick TiO_2 films. The red marker denotes edge dislocations. Insets are the corresponding FFT patterns.

orthorhombic distortion (i.e., b/a). The electrical conductivity (σ) is 2–3 S cm^{-1} and is independent of b/a [Fig. 4(a)]. Similar to the Nb concentration ($0.5\% \approx 1.6 \times 10^{20}$ cm^{-3}), the carrier concentration (n) is in the range of 10^{19}–10^{20} cm^{-3} and shows a gradual decreasing tendency as b/a increases [Fig. 4(b)]. For a semiconductor film depositing on sapphire, the band bending possibly occurs around the interface. Thus, the carriers within a contained thickness would be trapped, resulting in the decreasing of n when thickness decreased. In contrast, μ_{Hall} shows the opposite trend [Fig. 4(c)]. For a small b/a ratio (∼1.01), the μ_{Hall} value is ∼0.3 $cm^2\,V^{-1}\,s^{-1}$. μ_{Hall} increases with b/a and exceeds 1 $cm^2\,V^{-1}\,s^{-1}$ when $b/a = 1.034$. The variety of μ_{Hall} should be related to the change of effective mass, which would be revealed later.

It should be noted that the thermopower ($-S$) gradually decreases with b/a from ∼600 to ∼430 $\mu V\,K^{-1}$ [Fig. 4(d)]. According to Mott's formula, $-S$ reflects n for semiconductors; $-S$ decreases as n increases if the Fermi energy increases on the parabolic electronic density of states (DOS) and m^* is constant. Thus, the observed tendencies of $-S$ and n reveal that the m^* becomes lighter when orthorhombic lattice distortion is introduced.

For visualization, m^* is estimated from the relation between n and S as[39]

$$S = -\frac{k_B}{e}\left(\frac{(r+2)F_{r+1}(\xi)}{(r+1)F_r(\xi)} - \xi\right),$$

$$n = 4\pi\left(\frac{2m^* k_B T}{h^2}\right)^{3/2} F_{1/2}(\xi),$$

where k_B, r, F_r, ξ, T, and h are the Boltzmann constant, scattering parameter of the relaxation time, Fermi integral, chemical potential, absolute temperature, and Plank's constant, respectively. F_r can be further expressed as

$$F_r(\xi) = \int_0^\infty \frac{x^r}{1 + e^{x-\xi}} dx.$$

Figure 4(e) plots the estimated m^* as a function of b/a. m^* of the almost relaxed rutile TiO_2 film ($b/a \sim 1.008$) is ∼35 m_0. This value is consistent with the reported m^* of bulk rutile TiO_2 (12–35 m_0).[40–43] It should be noted that the m^* decreases as b/a

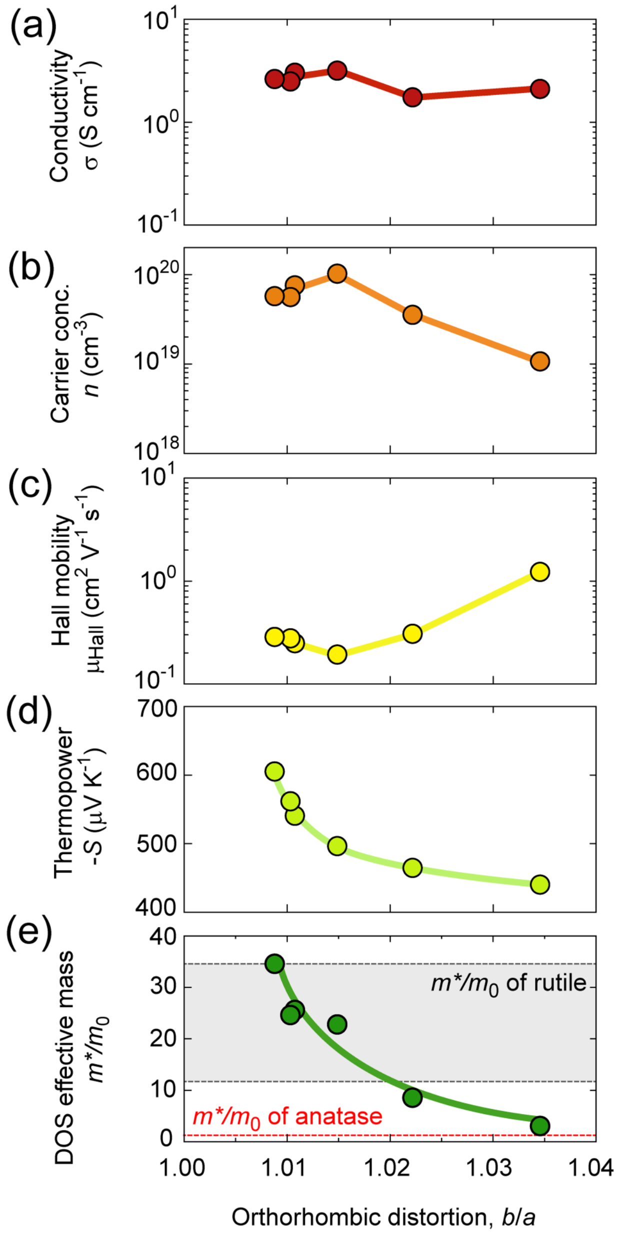

FIG. 4. Room temperature electron transport properties of the TiO_2 films as the function of orthorhombic distortion. (a) Electrical conductivity (σ), (b) carrier concentration (n), (c) Hall mobility (μ_{Hall}), (d) Thermopower (S), and (e) DOS effective mass (m^*/m_0). The gray region and red dotted line in (e) indicate the reported effective masses of rutile[40–43] and anatase TiO_2,[17,19] respectively. Solid lines are to guide the eye. Note that n decreases while |S| increases with b/a.

increases and reaches ~3 m_0 when $b/a = 1.034$. This smaller m^* is closer to that of anatase TiO_2 (~1 m_0).[17,19] So far, we demonstrated the relation between distortion and effective mass. The decreasing tendency is corresponding to the increase of mobility, revealing the major factor in the change of mobility.

In addition to the electron transport properties, E_g is also a property associated with the electronic structure. There is a consensus that the E_g of bulk rutile TiO_2 is ~3.06 eV while that of anatase is ~3.20 eV.[1,44,45] To clarify the effect of the orthorhombic distortion on E_g, we measured the optical transmission and reflection spectra of the resultant films (Fig. S10 in the supplementary material). It should be noted that, although rutile TiO_2 is a direct bandgap semiconductor, the direct transition is dipole-forbidden and degenerated with the indirect allowed transition.[46–48] Thus, direct E_g is equivalent to indirect E_g and was possible to be evaluated by extrapolating the linear region of the Tauc $[(\alpha h\nu)^{1/2} - h\nu]$ plot (Fig. S11 in the supplementary material). E_g gradually increases from ~3.11 to ~3.48 eV as b/a increases [Fig. 5(a)]. Even a highly relaxed film (300 nm) shows a small distortion ($b/a \sim 1.008$), which may explain why E_g is slightly higher than the rutile bulk value (~3.06 eV).[49]

Generally, the E_g of an extremely thin layer is greater than that of the bulk due to the quantum size effect (QSE). QSE occurs

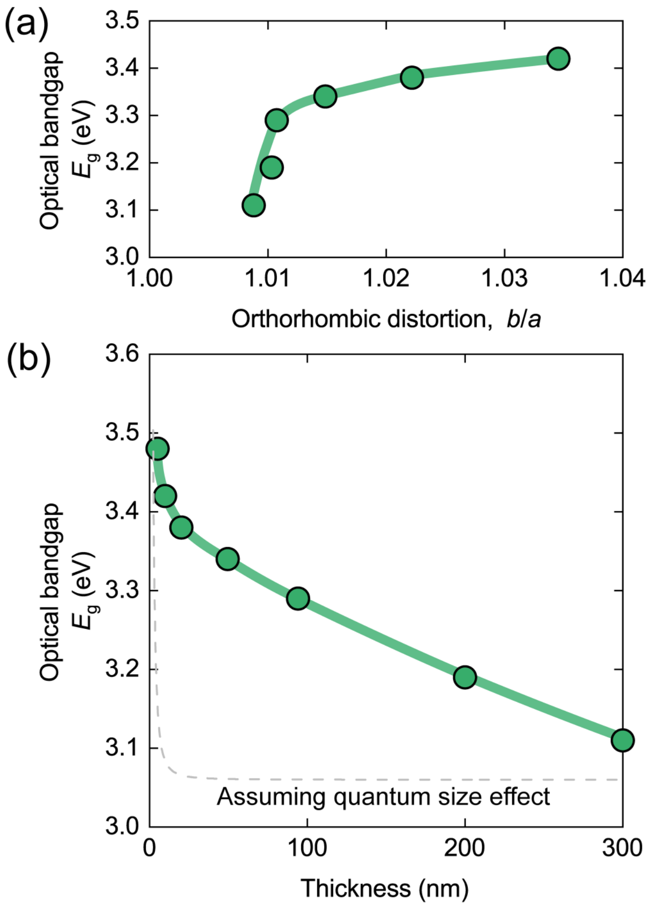

FIG. 5. Denying the quantum size effect of TiO_2 epitaxial films. Change in E_g of the TiO_2 films. (a) E_g increases with b/a. (b) E_g increases as the thickness decreases. This increasing tendency completely differs from the assumption for the quantum size effect.

when the film thickness is thinner than the de Broglie wavelength. E_g gradually increases as the film thickness decreases [Fig. 5(b)]. To clarify the origin of the increased E_g, we calculated E_g assuming that QSE can be expressed as[50,51]

$$E_g = E_{g,\,Bulk} + \frac{h^2}{2d^2}\left(\frac{1}{m_e^*}+\frac{1}{m_h^*}\right),$$

where $E_{g,\,Bulk}$, h, and d are the bulk bandgap, Planck's constant, and film thickness, respectively. m_e* and m_h* are the electron and hole effective masses, which are assumed to be ∼20[41] and ∼5 m_0,[52] respectively. The calculated E_g increases dramatically when the film thickness is thinner than ∼10 nm. This behavior does not fit with the observed E_g, indicating that the QSE theory cannot explain the observed E_g. These observations confirm that the electronic structure of a rutile TiO_2 film is predominantly modulated via orthorhombic distortion.

Nb:TiO_2 films grown on $(1\bar{1}00)$ α-Al_2O_3 substrate show differentiated properties from the rutile phase when the thickness is sufficiently thin due to orthorhombic lattice distortion but typical properties of the rutile phase appear as the thickness increases. Since rutile Nb:TiO_2 shows interesting transport properties at low temperatures and the temperature-related behavior may provide information about the transport mechanism, we measured the temperature dependence of the electron transport properties of the 300-nm-thick Nb:TiO_2 film ($b/a \sim 1.008$) and the 20-nm-thick Nb:TiO_2 film ($b/a = 1.034$). Both films show semiconductor-like behaviors of ρ [Fig. 6(a)]. As the temperature decreases, ρ gradually increases, n gradually decreases [Fig. 6(b)], and μ_{Hall} increases [Fig. 6(c)]. These results suggest that phonons dominate carrier scattering.

The films display different temperature dependences of $-S$ [Fig. 6(d)]. At room temperature, the $-S$ values of the 300- and the 20-nm-film are ∼0.6 and 0.45 mV K^{-1}, respectively. As the temperature decreases, the former increases dramatically and exceeds 1.5 mV K^{-1}. In contrast, the latter decreases gradually and approaches zero. It has been observed that rutile TiO_2 shows a colossal $-S$ at low temperature due to the phonon drag effect.[40,53] This behavior is usually observed in materials with a large m*.[54–57] As above described, m* of the 300-nm-film is 35 m_0 while that of the 20-nm-film is ∼3 m_0. Similarly, the presence or absence of a colossal $-S$ reflects the distortion-induced m* modulation at room temperature.

These observations reveal that introducing orthorhombic lattice distortion using $(1\bar{1}00)$ α-Al_2O_3 substrates significantly modulates the electronic structure of rutile TiO_2. Orthorhombic distortion realizes changes in E_g, m*, and $-S$, indicating that the electronic structure of rutile TiO_2 shifts toward that of anatase TiO_2.

C. Changes in the electronic structure of rutile TiO_2 due to orthorhombic distortion

The XAS spectra of the TiO_2 films were measured to directly clarify the change in the electronic structure of rutile TiO_2 upon orthorhombic distortion. Figure 7 shows the XAS spectra of the 10–200-nm-thick rutile TiO_2 films at the Ti L_3-edge. The single peak around ∼456 eV corresponds to the threefold degenerate t_{2g} state, and the double peak around ∼459 eV corresponds to the twofold degenerate e_g state. The e_g peak is further split into two peaks (e_{g1} and e_{g2}) due to the octahedral distortion of TiO_6 octahedra. The octahedral distortion differs between rutile and anatase. Rutile is D_{2h} symmetry, while anatase is D_{2d}. This difference is reflected in the XAS spectra as the inversion of the relative intensities of the e_{g1} and e_{g2} peaks. Hence, their intensities can be used as a fingerprint for different TiO_2 polymorphs (Fig. S12 in the supplementary material).[58] The observed XAS spectra indicate that the TiO_2 films maintain the electronic structure of the rutile phase. Although the anatase phase does not appear even with a

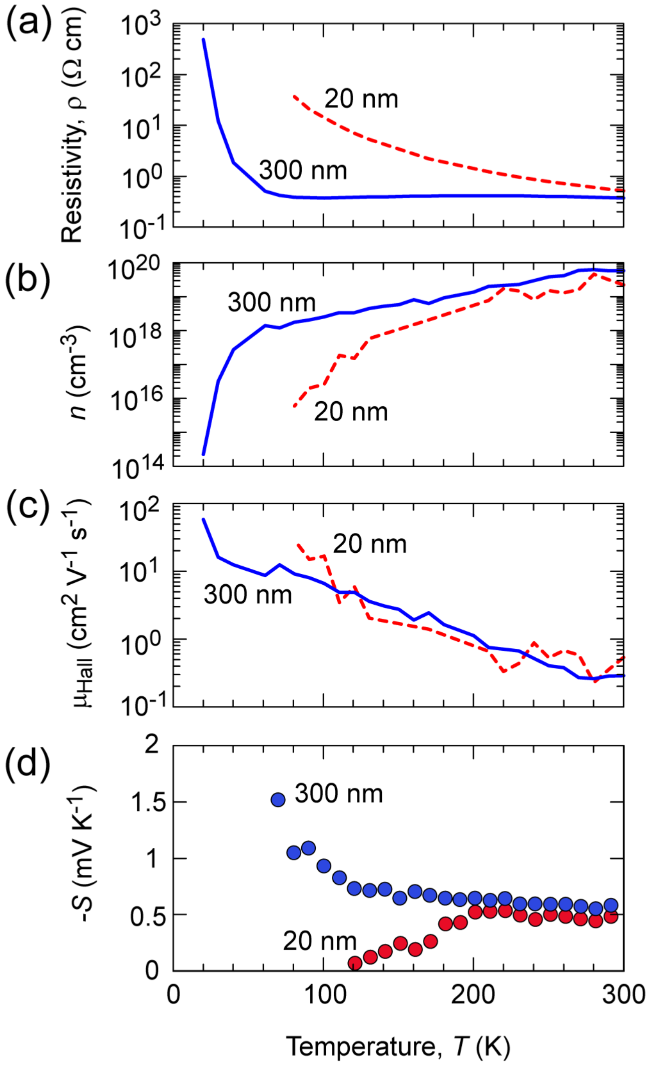

FIG. 6. Low-temperature electron transport properties of the TiO_2 films. (a) Resistivity, (b) carrier concentration (n), (c) Hall mobility (μ_{Hall}), and (d) thermopower (S) of 20- and 300-nm-thick rutile TiO_2 films grown on $(1\bar{1}00)$ α-Al_2O_3 substrates. Note that the $|S|-T$ curve of the 300-nm-thick TiO_2 is similar to that of the reduced rutile TiO_2 single crystal, whereas that of the 20-nm-thick TiO_2 is similar to that of the anatase TiO_2 epitaxial film.

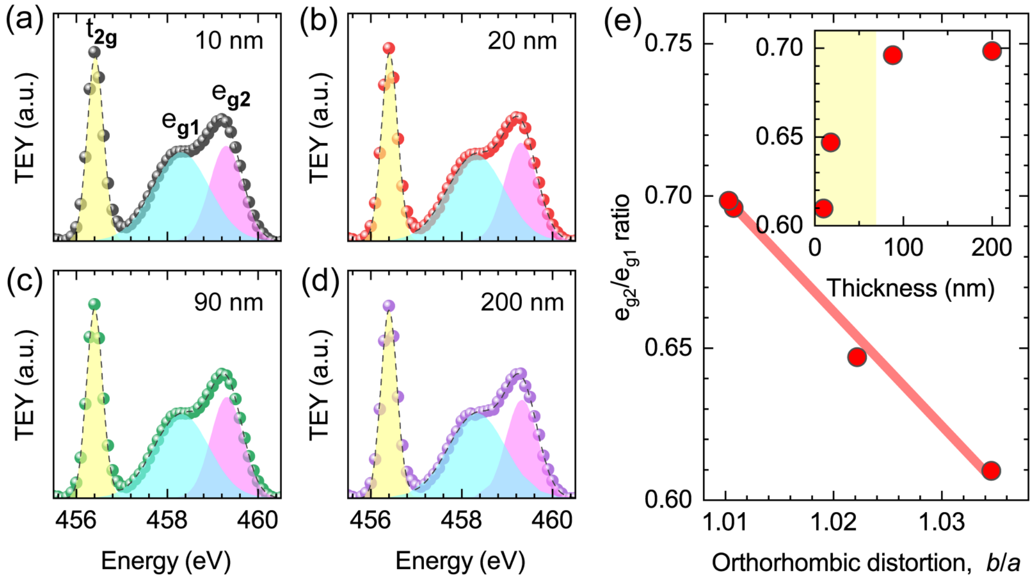

FIG. 7. Ti L_3 XAS spectra of the 10–200-nm-thick rutile TiO_2 films. (a) 10-nm-thick TiO_2, (b) 20-nm-thick TiO_2, (c) 90-nm-thick TiO_2, and (d) 200-nm-thick TiO_2 grown on $(1\bar{1}00)$ α-Al_2O_3 substrates. Peak fitting is processed by the Gaussian distribution. (e) Relative peak area ratio of e_{g2}/e_{g1} as a function of orthorhombic distortion. The inset plots the e_{g2}/e_{g1} ratio as a function of the film thickness.

large orthorhombic distortion, we consider that changes in the lattice parameters result in changes in the degree of octahedral distortion. This small perturbation has a non-negligible effect on the physical properties.[9,59,60] From this viewpoint, we fitted the XAS data into a Gaussian distribution (the fitting parameters were available in Table S1 in the supplementary material) and calculated the relative peak area ratio of e_{g2}/e_{g1} [Figs. 7(a)–7(d)]. As the thickness increases, e_{g2}/e_{g1} shows an increasing tendency [Fig. 7(e), inset]. However, e_{g2}/e_{g1} linearly decreases as b/a increases [Fig. 7(e)], clearly indicating that there is a strong correlation between the electronic structure of rutile TiO_2 and the orthorhombic lattice distortion.

D. DFT calculation of TiO_2 with orthorhombic lattice distortion

Finally, DFT calculations of rutile TiO_2 with orthorhombic lattice distortion were performed to investigate the influence of lattice distortion of TiO_2 thin films on electron m^*. Three TiO_2 unit cells were considered: (1) a rutile unit cell with fully optimized a- and c-axis lengths (a_0, $b_0 = a_0$, c_0), (2) a rutile unit cell with the b-axis length extended 3% from the fully optimized value (a_0, $1.030b_0$, c_0), and (3) a rutile unit cell with the a-axis length compressed 0.5% and the b-axis length extended 3% ($0.995a_0$, $1.03b_0$, $0.994c_0$). These extensions and compressions of a_0 and b_0 are based on the experimental data shown in Fig. 2. It should be noted that the c-axis length in case 3 was optimized by the DFT calculations, and the optimized c-axis length of $0.994c_0$ agrees well with that for the thin-film value (about $0.9925c_0$) shown in Fig. 2(c). Moreover, the theoretical E_g value for the distorted unit cell (case 3) is 2.37 eV, which is larger than the fully optimized unit cell value of 2.30 eV. The increased E_g trend for the distorted rutile unit cell agrees well with the experimental E_g variation against orthogonal distortion shown in Fig. 5(a).

Table I lists the calculated m^* values at the Γ point toward the X (or Y) point and the M (or S) point (these directions correspond to the in-plane ones to the thin-film surface). The DFT results show that the m^*'s of the fully optimized rutile TiO_2 are around 1.7 and 0.6 m_0, which are much smaller than the experimentally observed value (∼35 m_0). Previous GGA calculations provided similar theoretical results.[47,61,62] It is thought that electronic conduction in rutile TiO_2 is not simply described by the m^*-like states, but is strongly affected by the formation of polarons, namely, electron coupling with lattice vibrations (phonons). As the orthogonal distortions increase (cases 2 and 3), the calculated m^* values tend to increase. However, the m^* values are still smaller than the experimentally observed one (3 m_0) for the distorted thin films [Fig. 4(e)]. Hence, it is most likely that the original orthogonal distortions of the rutile TiO_2 thin films due to the substrate considerably change the lattice vibrational states in the thin films.

IV. CONCLUSION

Nb-doped rutile TiO_2 epitaxial films on $(1\bar{1}00)$ α-Al_2O_3 substrate exhibit anatase-like optoelectronic properties due to orthorhombic lattice distortions. As the film thickness decreases, b/a increases up to 3.4%. As b/a increases, the carrier m^* decreases from 35 to 3 m_0 (m_0: electron mass) but E_g increases. The electronic structure change was observed experimentally. The present observations provide insight into regulating the physical properties of TiO_2 and should aid in the design of TiO_2-based photocatalysts and transparent conducting electrodes.

SUPPLEMENTARY MATERIAL

See the supplementary material for x-ray reciprocal space mappings (RSMs) around (left) $(3\bar{3}06)$ α-Al_2O_3 and (right) $(4\bar{2}\bar{2}0)$ α-Al_2O_3 diffraction spots of the TiO_2 film (300, 200, 100, 50, 20, and 10 nm) grown on $(1\bar{1}00)$ α-Al_2O_3 substrates. Optical transmission and reflection spectra of the 5–300-nm-thick TiO_2 films grown on $(10\bar{1}0)$ α-Al_2O_3 substrates and Tauc plots ($(\alpha h\nu)^{1/2} - h\nu$) of the 5–300-nm-thick rutile TiO_2 films grown on $(1\bar{1}00)$ α-Al_2O_3 substrates.

ACKNOWLEDGMENTS

This research was supported by Grants-in-Aid for Innovative Areas (Nos. 19H05791, 19H05786, and 19H05788) from the JSPS. B.C. was supported by a MEXT scholarship. A part of this work was supported by the Crossover Alliance to Create the Future with People, Intelligence and Materials and by the Network Joint Research Center for Materials and Devices. H.O. was supported by a Grant-in-Aid for Scientific Research A (No. 22H00253). H.J. and K.K. are supported by the international cooperation program by the NRF (No. NRF-2018K2A9A2A08000079). Y.Z. was supported by the Start-Up Fund of Jiangsu University (No. 5501310015), Guangdong Basic and Applied Basic Research Foundation (No. 2021A1515110881), and the Youth Fund of Foshan (Southern China) Institute for New Materials (No. 2021AYF25009). J.L. was supported by Grant-in-Aid for JSPS Fellows. A part of this work was supported by the Advanced Research Infrastructure for Materials and Nanotechnology Japan (Grant No. JPMXP1222UT0055) by MEXT.

AUTHOR DECLARATIONS

Conflict of Interest

The authors have no conflicts to disclose.

Author Contributions

B.C. prepared the samples and conducted the measurements. K.K. and H.J. performed the XAS measurements and analyses. Y.Z. analyzed the effective mass. J.L., B.F., and Y.I. performed the STEM observations and analyses. S.H and K.M. performed DFT calculations. B.C. and H.O. planned and supervised the project. All authors discussed the results and commented on the manuscript.

Binjie Chen: Conceptualization (equal); Data curation (equal); Formal analysis (equal); Investigation (equal); Validation (equal); Writing – original draft (equal); Writing – review & editing (equal). **Kungwan Kang:** Investigation (equal); Writing – review & editing (equal). **Hyoungjeen Jeen:** Investigation (equal); Writing – review & editing (equal). **Yuqiao Zhang:** Investigation (equal); Validation (equal); Writing – review & editing (equal). **Jinghuang Lin:** Investigation (equal); Writing – review & editing (equal). **Bin Feng:** Investigation (equal); Writing – review & editing (equal). **Yuichi Ikuhara:** Investigation (equal); Writing – review & editing (equal). **Sena Hoshino:** Investigation (equal); Writing – review & editing (equal). **Katsuyuki Matsunaga:** Investigation (equal); Writing – review & editing (equal). **Hiromichi Ohta:** Conceptualization (equal); Data curation (equal); Funding acquisition (equal); Project administration (equal); Supervision (equal); Writing – original draft (equal); Writing – review & editing (equal).

DATA AVAILABILITY

The data that support the findings of this study are available from the corresponding author on reasonable request.

REFERENCES

[1] C. Dette, M. A. Perez-Osorio, C. S. Kley, P. Punke, C. E. Patrick, P. Jacobson, F. Giustino, S. J. Jung, and K. Kern, Nano Lett. **14**, 6533 (2014).
[2] V. Etacheri, C. Di Valentin, J. Schneider, D. Bahnemann, and S. C. Pillai, J. Photochem. Photobiol. C **25**, 1 (2015).
[3] R. V. Nair, V. S. Gummaluri, M. V. Matham, and C. Vijayan, J. Phys. D: Appl. Phys. **55**, 313003 (2022).
[4] A. Fujishima and K. Honda, Nature **238**, 37 (1972).
[5] R. Daghrir, P. Drogui, and D. Robert, Ind. Eng. Chem. Res. **52**, 3581 (2013).
[6] J. Schneider, M. Matsuoka, M. Takeuchi, J. L. Zhang, Y. Horiuchi, M. Anpo, and D. W. Bahnemann, Chem. Rev. **114**, 9919 (2014).
[7] Y. C. Lan, Y. L. Lu, and Z. F. Ren, Nano Energy **2**, 1031 (2013).
[8] M. E. Arroyo-de Dompablo, A. Morales-Garcia, and M. Taravillo, J. Chem. Phys. **135**, 054503 (2011).
[9] Y. X. Hu, Y. Y. Pan, Z. L. Wang, T. G. Lin, Y. Y. Gao, B. Luo, H. Hu, F. T. Fan, G. Liu, and L. Z. Wang, Nat. Commun. **11**, 2129 (2020).
[10] N. Rahimi, R. A. Pax, and E. M. Gray, Prog. Solid State Chem. **44**, 86 (2016).
[11] T. Luttrell, S. Halpegamage, J. Tao, A. Kramer, E. Sutter, and M. Batzill, Sci. Rep. **4**, 4043 (2014).
[12] M. Nishikawa, S. Yuto, T. Nakajima, T. Tsuchiya, and N. Saito, Catal. Lett. **147**, 292 (2017).
[13] D. A. H. Hanaor and C. C. Sorrell, J. Mater. Sci. **46**, 855 (2011).
[14] Z. H. Cui, F. Wu, and H. Jiang, Phys. Chem. Chem. Phys. **18**, 29914 (2016).
[15] L. J. Liu, H. L. Zhao, J. M. Andino, and Y. Li, ACS Catal. **2**, 1817 (2012).
[16] T. Hitosugi, N. Yamada, S. Nakao, Y. Hirose, and T. Hasegawa, Phys. Status Solidi A **207**, 1529 (2010).
[17] H. Tang, K. Prasad, R. Sanjines, P. E. Schmid, and F. Levy, J. Appl. Phys. **75**, 2042 (1994).
[18] A. Lotnyk, S. Senz, and D. Hesse, Thin Solid Films **515**, 3439 (2007).
[19] D. Kurita, S. Ohta, K. Sugiura, H. Ohta, and K. Koumoto, J. Appl. Phys. **100**, 096105 (2006).
[20] R. J. Kennedy and P. A. Stampe, J. Cryst. Growth **252**, 333 (2003).
[21] S. J. Zheng, C. A. J. Fisher, T. Kato, Y. Nagao, H. Ohta, and Y. Ikuhara, Appl. Phys. Lett. **101**, 191602 (2012).
[22] S. Yamamoto, T. Sumita, T. Yamaki, A. Miyashita, and H. Naramoto, J. Cryst. Growth **237**, 569 (2002).
[23] E. Breckenfeld, H. Kim, K. Burgess, N. Charipar, S. F. Cheng, R. Stroud, and A. Pique, ACS Appl. Mater. Interfaces **9**, 1577 (2017).
[24] B. J. Chen, G. Kim, H. J. Cho, and H. Ohta, Adv. Electron. Mater. **8**, 2100687 (2022).
[25] J. Li, F. Li, Y. Zhuang, L. Jin, L. Wang, X. Wei, Z. Xu, and S. Zhang, J. Appl. Phys. **116**, 074105 (2014).
[26] H. Usui, S. Yoshioka, K. Wasada, M. Shimizu, and H. Sakaguchi, ACS Appl. Mater. Interfaces **7**, 6567 (2015).
[27] P. E. Blochl, Phys. Rev. B **50**, 17953 (1994).
[28] G. Kresse and J. Hafner, Phys. Rev. B **48**, 13115 (1993).
[29] J. P. Perdew, K. Burke, and M. Ernzerhof, Phys. Rev. Lett. **77**, 3865 (1996).

[30] S. L. Dudarev, G. A. Botton, S. Y. Savrasov, C. J. Humphreys, and A. P. Sutton, Phys. Rev. B **57**, 1505 (1998).
[31] X. P. Han and G. S. Shao, J. Phys. Chem. C **115**, 8274 (2011).
[32] C. J. Howard, T. M. Sabine, and F. Dickson, Acta Crystallogr. B **47**, 462 (1991).
[33] H. A. Huy, B. Aradi, T. Frauenheim, and P. Deak, Phys. Rev. B **83**, 155201 (2011).
[34] H. Tang, F. Levy, H. Berger, and P. E. Schmid, Phys. Rev. B **52**, 7771 (1995).
[35] J. Heyd, G. E. Scuseria, and M. Ernzerhof, J. Chem. Phys. **118**, 8207 (2003).
[36] A. V. Krukau, O. A. Vydrov, A. F. Izmaylov, and G. E. Scuseria, J. Chem. Phys. **125**, 224106 (2006).
[37] X. Sun, D. Wu, L. Zou, S. D. House, X. Chen, M. Li, D. N. Zakharov, J. C. Yang, and G. Zhou, Nature **607**, 708 (2022).
[38] Z. Zhang, Y. Long, S. Cazottes, R. Daniel, C. Mitterer, and G. Dehm, Sci. Rep. **5**, 11460 (2015).
[39] C. B. Vining, J. Appl. Phys. **69**, 331 (1991).
[40] W. R. Thurber and A. J. H. Mante, Phys. Rev. **139**, A1655 (1965).
[41] M. Itakura, N. Niizeki, H. Toyoda, and H. Iwasaki, Jpn. J. Appl. Phys. **6**, 311 (1967).
[42] H. Frederikse, J. Appl. Phys. **32**, 2211 (1961).
[43] J. W. Deford and O. W. Johnson, J. Appl. Phys. **54**, 889 (1983).
[44] L. Kavan, M. Gratzel, S. E. Gilbert, C. Klemenz, and H. J. Scheel, J. Am. Chem. Soc. **118**, 6716 (1996).
[45] D. O. Scanlon, C. W. Dunnill, J. Buckeridge, S. A. Shevlin, A. J. Logsdail, S. M. Woodley, C. R. A. Catlow, M. J. Powell, R. G. Palgrave, I. P. Parkin, G. W. Watson, T. W. Keal, P. Sherwood, A. Walsh, and A. A. Sokol, Nat. Mater. **12**, 798 (2013).
[46] H. Mathieu, J. Pascual, and J. Camassel, Phys. Rev. B **18**, 6920 (1978).
[47] C. E. Ekuma and D. Bagayoko, Jpn. J. Appl. Phys. **50**, 101103 (2011).
[48] Y. Yamada and Y. Kanemitsu, Phys. Rev. B **82**, 113103 (2010).
[49] P. R. Huang, Y. He, C. Cao, and Z. H. Lu, Sci. Rep. **4**, 7131 (2014).
[50] D. J. Lockwood, Z. H. Lu, and J. M. Baribeau, Phys. Rev. Lett. **76**, 539 (1996).
[51] D. D. Liang, B. J. Chen, H. J. Cho, and H. Ohta, ACS Appl. Electron. Mater. **2**, 3454 (2020).
[52] S. Dong, S. Xia, C. Wang, J. Dong, T. Wang, R. Li, Z. Ren, D. Dai, X. Yang, and C. Zhou, J. Phys. Chem. Lett. **13**, 2299 (2022).
[53] J. K. Tang, W. D. Wang, G. L. Zhao, and Q. Li, J. Phys.: Condens. Matter **21**, 205703 (2009).
[54] H. Takahashi, R. Okazaki, S. Ishiwata, H. Taniguchi, A. Okutani, M. Hagiwara, and I. Terasaki, Nat. Commun. **7**, 12732 (2016).
[55] H. P. R. Frederikse, W. R. Thurber, and W. R. Hosler, Phys. Rev. **134**, A442 (1964).
[56] H. Matsuura, H. Maebashi, M. Ogata, and H. Fukuyama, J. Phys. Soc. Jpn. **88**, 074601 (2019).
[57] O. V. Emelyanenko, E. E. Klotinsh, D. N. Nasledov, and V. G. Sidorov, Phys. Status Solidi **12**, K89 (1965).
[58] R. Ruus, A. Kikas, A. Saar, A. Ausmees, E. Nommiste, J. Aarik, A. Aidla, T. Uustare, and I. Martinson, Solid State Commun. **104**, 199 (1997).
[59] X. H. Zhang, C. L. Pei, X. Chang, S. Chen, R. Liu, Z. J. Zhao, R. T. Mu, and J. L. Gong, J. Am. Chem. Soc. **142**, 11540 (2020).
[60] G. C. Vasquez, D. Maestre, A. Cremades, J. Ramirez-Castellanos, E. Magnano, S. Nappini, and S. Z. Karazhanov, Sci. Rep. **8**, 8740 (2018).
[61] H. Kamisaka, T. Hitosugi, T. Suenaga, T. Hasegawa, and K. Yamashita, J. Chem. Phys. **131**, 034702 (2009).
[62] J. F. Zhang, P. Zhou, J. J. Liu, and J. G. Yu, Phys. Chem. Chem. Phys. **16**, 20382 (2014).